nature astronomy

Article

https://doi.org/10.1038/s41550-023-02119-1

Gamma rays from a reverse shock with turbulent magnetic fields in GRB 180720B

Received: 6 February 2023

Accepted: 2 October 2023

Published online: 23 November 2023

Check for updates

Makoto Arimoto[1], Katsuaki Asano[2], Koji S. Kawabata[3,4], Kenji Toma[5,6], Ramandeep Gill[7,8], Jonathan Granot[8,9,10], Masanori Ohno[3,4], Shuta Takahashi[1], Naoki Ogino[1], Hatsune Goto[1], Kengo Nakamura[4], Tatsuya Nakaoka[3,4], Kengo Takagi[4], Miho Kawabata[4,11], Masayuki Yamanaka[3,12], Mahito Sasada[3,13] & Soebur Razzaque[10,14]

Gamma-ray bursts (GRBs) are the most electromagnetically luminous cosmic explosions. They are powered by collimated streams of plasma (jets) ejected by a newborn stellar-mass black hole or neutron star at relativistic velocities. Their short-lived (typically tens of seconds) prompt γ-ray emission from within the ejecta is followed by long-lived multi-wavelength afterglow emission from the ultra-relativistic forward shock. This shock is driven into the circumburst medium by the GRB ejecta. which are in turn decelerated by a mildly relativistic reverse shock. Forward-shock emission was recently detected as teraelectronvolt-energy γ-rays. Such very-high-energy emission was also predicted from the reverse shock. Here we report the detection of optical and gigaelectronvolt-energy γ-ray emission from GRB 180720B during the first few hundred seconds, which is explained by synchrotron and inverse-Compton emission from the reverse shock propagating into the ejecta, implying a low-magnetization ejecta. Our optical measurements show a clear transition from the reverse shock to the forward shock driven into the circumburst medium, accompanied by a 90° change in the mean polarization angle and fluctuations in the polarization degree and angle. This indicates turbulence with large-scale toroidal and radially stretched magnetic-field structures in the reverse and forward shocks, respectively, which tightly couple to the physics of relativistic shocks and GRB jets, namely launching, composition, dissipation and particle acceleration.

On 20 July 2018, the Fermi Gamma-ray Burst Monitor and Swift Burst Alert Telescope (Swift-BAT) were triggered by and localized the γ-ray burst (GRB) GRB 180720B at a redshift of $z = 0.654$ (ref. 1; a luminosity distance of 4.0 Gpc), with a time-integrated isotropic equivalent energy of $E_{\rm iso} = 5 \times 10^{53}$ erg (1–10^4 keV) and a duration of ~60 s (Supplementary Information). These observations were followed by multi-wavelength observations from radio to teraelectronvolt energies: radio, optical, X-ray, gigaelectronvolt and teraelectronvolt[2]. The Fermi Large Area Telescope (Fermi-LAT) covered the gigaelectronvolt band (Methods). The light curves observed in different energy bands are shown in Fig. 1.

Following the alert of the GRB position by Swift, the Kanata 1.5 m telescope performed follow-up observations[3]. Equipped with optical polarimetry instruments (HOWPol and HONIR), it detected bright optical emissions ~100 s after the burst trigger (GRB trigger time represented as T_0). Fermi-LAT also detected bright gigaelectronvolt

A full list of affiliations appears at the end of the paper. e-mail: arimoto@se.kanazawa-u.ac.jp

https://doi.org/10.1038/s41550-023-02119-1

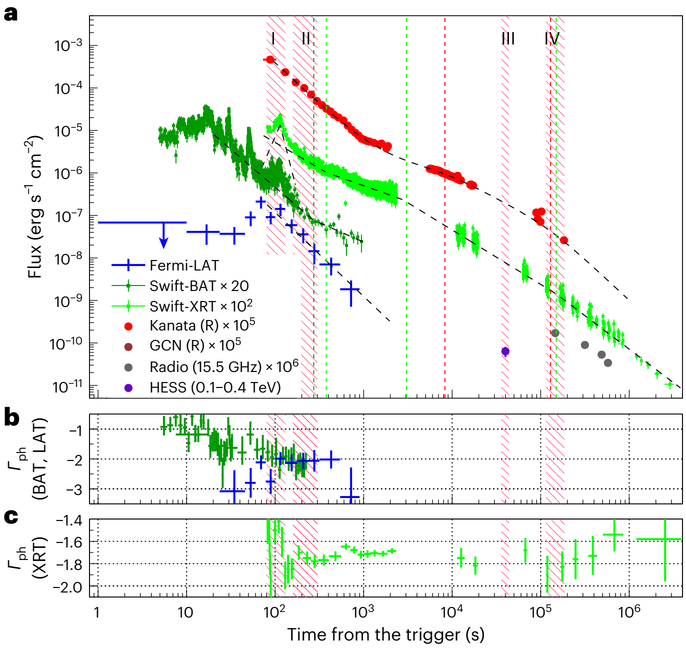

Fig. 1 | Light curves from the radio to teraelectronvolt bands of GRB 180720B. **a**, Unabsorbed light curves of GRB 180720B from Fermi-LAT (0.1–1 GeV), Swift-BAT (15–150 keV), Swift-XRT (0.3–10 keV), Kanata and other telescopes, namely General Coordinates Network (GCN; approximately electronvolts), Arcminute Microkelvin Imager Large Array (15.5 GHz) and High Energy Stereoscopic System (HESS; 0.1–0.4 TeV). The black dashed lines represent the best-fitting power-law functions with breaks and the vertical dashed lines represent the corresponding break times. **b**, The observed photon indices observed by Swift-BAT (dark green) and Fermi-LAT (blue). **c**, The observed photon indices observed by Swift-XRT (green). All error bars correspond to the 1σ confidence region.

emissions peaking at T_0 + ~100 s. In the early phase (T_0 + 100 s to T_0 + 1,000 s), the optical ($F_{\rm opt} \propto t^{\alpha_{\rm opt}}$) and gigaelectronvolt ($F_{\rm GeV} \propto t^{\alpha_{\rm GeV}}$) fluxes declined with temporal indices of $\alpha_{\rm opt} = -1.94 \pm 0.08$ and $\alpha_{\rm GeV} = -1.91 \pm 0.31$, respectively, showing a similar trend. Both values are much steeper than the typical temporal index of GRB afterglows[4,5], indicating rapidly fading emission originating from a reverse shock. During the subsequent time, the optical temporal index became $\alpha_{\rm opt} = -1.10 \pm 0.02$ (Methods), which is a typical index for emissions coming from the forward shock. Our optical polarization measurements by HOWPol and HONIR during T_0 + 70 s to T_0 + 20,000 s cover both the reverse and forward shock dominated phases (Fig. 2). They reveal that the polarization degree (PD) and polarization angle (PA) were changing gradually (PD $\lesssim$ 1% to 8% and PA $\simeq$ 50° to ~150°) during the initial 1,000 s interval after the burst. In the late phase ($t_{\rm obs} > T_0$ + 5,000 s), almost constant PD and PA (~1% with ~160°) were detected (Supplementary Information for the analysis details). The detection of optical polarization from the reverse and forward shocks in a single GRB is unprecedented[6] and may be a powerful probe of the structure and origin of magnetic fields in the shocked regions.

First, to better understand the rapid fading in the early phase, we extracted wideband (optical to gigaelectronvolt) spectral energy distributions (SEDs) from T_0 + 80 s to T_0 + 300 s (Fig. 3). Specifically in the time interval T_0 + 160 s to T_0 + 300 s (interval II), the optical and gigaelectronvolt components are distinctly higher than the extrapolations from the X-ray component, which probably originated from the forward shock (see Supplementary Information for the significance of the gigaelectronvolt excess). Thus, to explain the optical and gigaelectronvolt excesses, an additional component, such as a reverse-shock component, is needed. Note that in the time interval T_0 + 80 s to T_0 + 130 s (interval I), the flux contribution from a bright X-ray flare at T_0 + ~100 s is substantial and the X-ray flare probably comes from a different emission site, as indicated by the short variability timescales (see Methods for a discussion of the X-ray flare).

The gigaelectronvolt onset timescale of ~100 s roughly corresponds to the time required for the reverse shock to cross the ejecta shell, and since the prompt emission lasts ~60 s, this implies that the reverse shock is mildly relativistic[7]. The bright optical emission can be explained by synchrotron emission from the reverse shock in the slow-cooling regime[8]. However, after the reverse shock crosses the ejecta shell, there is no injection of freshly accelerated power-law electrons into the shocked shell. As a result, synchrotron emission above the synchrotron cooling frequency sharply drops, so that the typical cooling frequency reaches the X-ray band at most[8]. Thus, the observed γ-rays cannot be powered by synchrotron emission and are potentially produced by synchrotron self-Compton (SSC) emission in the reverse shock[9–11], with seed optical photons inverse-Compton scattered to gigaelectronvolt energies by the same shock-accelerated electrons emitting the optical photons. The theoretical temporal index of the SSC emission from the reverse shock is almost the same as that of the synchrotron emission (Methods). Several works have already reported possible SSC emission from the reverse shock[12–16], although these works relied on only a few simultaneous optical observations to characterize both the reverse and forward shocks distinctly for the first few thousand seconds.

Because the intensity of the SSC emission depends on the fraction of the internal energy held by the electrons ($\epsilon_{e,r}$) and the magnetic field ($\epsilon_{B,r}$) in the reverse shock[4], the observed γ-ray emission can constrain these two microphysical parameters. To reproduce the observed SSC-to-synchrotron flux ratio ($Y \simeq 6$) of the SED in interval II, a small value of $\epsilon_{B,r}$ is required ($\epsilon_{B,r} \simeq 10^{-4}$–$10^{-3}$; Methods and Extended Data Table 1). The theoretical models fit well the observed optical and gigaelectronvolt fluxes, as shown in Fig. 3 and Extended Data Figs. 1 and 2. Due to the soft spectrum in the gigaelectronvolt band observed by Fermi-LAT, our modelling suggests a low value of the maximum electron energy in the reverse-shock region. The particle acceleration efficiency would be suppressed in the reverse-shock region compared to that in the forward shock (Methods). However, because the uncertainty of the Fermi-LAT spectrum is relatively large, future simultaneous observations by teraelectronvolt Cherenkov telescopes, such as MAGIC and the Cherenkov Telescope Array[17], during the early phase of the GRB afterglow will give a stringent limit on this process.

In the late phase ($t_{\rm obs} \gtrsim T_0$ + 5,000 s), emission from the reverse shock does not contribute to the observed fluxes due to its steep temporal decline, and forward-shock emission is dominant. Our analytical model with synchrotron and SSC emission in the forward shock matches the observed spectrum from the optical to very-high-energy band in interval III, as shown in Extended Data Fig. 3. (For more details of the synchrotron and SSC emission and its modelling, see Methods.) Thus, our results indicate that GRB 180720B is the very first GRB event showing the apparent SSC components observed from the reverse shock in the early phase and the forward shock in the late phase. In either case, the required magnetic parameter is low, $\epsilon_B \simeq 10^{-4}$–$10^{-3}$ (Methods and Extended Data Table 1). Although some previous works predicted a larger magnetization of the reverse shock compared with the forward shock due to the injection of a magnetized ejecta from the fireball[18], to be able to explain the strong SSC emission, our model requires the estimated magnetization of the forward and reverse shocks to be within the same order of magnitude. Thus, the high-energy γ-ray emission provides interesting constraints on the magnetization of the ejecta. The polarization measurement reveals the magnetic structure and its origin in the shocked regions.

The scenario with the reverse-shock emission is supported by the measured optical polarization. At $t_{\rm obs} \simeq T_0$ + 80 s to T_0 + 300 s when emission from the reverse shock dominates the flux, the PD changes gradually from ~5% to $\lesssim$1% whereas the PA remains roughly constant

https://doi.org/10.1038/s41550-023-02119-1

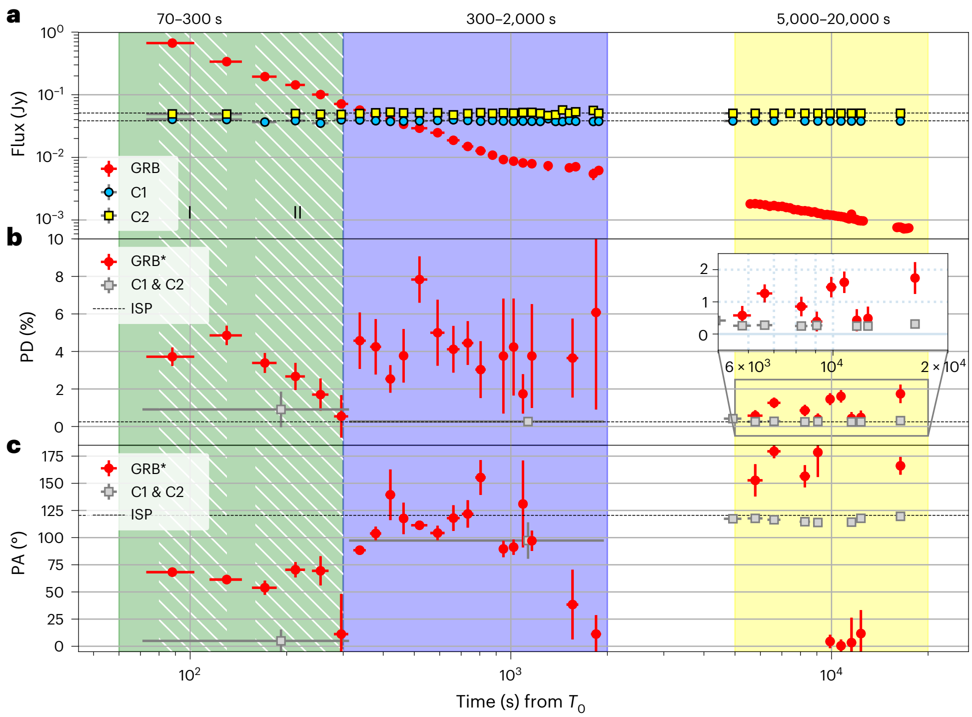

Fig. 2 | Optical lights curve, PDs and PAs of GRB 180720B and nearby stars. **a**, Optical light curves of GRB 180720B and the nearby stars (C1 and C2) observed by HOWPol and HONIR implemented on the Kanata telescope. **b**, PDs of GRB 180720B and the average of the nearby stars (C1 and C2). The inset shows a zoomed plot of the observed PD points of this GRB, C1 and C2. **c**, PAs of GRB 180720B and the average of the nearby stars (C1 and C2). An asterisk indicates intrinsic GRB polarization after subtraction of the interstellar polarization (ISP). HOWPol and HONIR covered $T_0 + 70$ s to $T_0 + 2{,}000$ s and $T_0 + 5{,}000$ s to $T_0 + 20{,}000$ s, respectively. The hatched areas represent the time intervals (I and II) shown in Fig. 1. All error bars correspond to the 1σ confidence region.

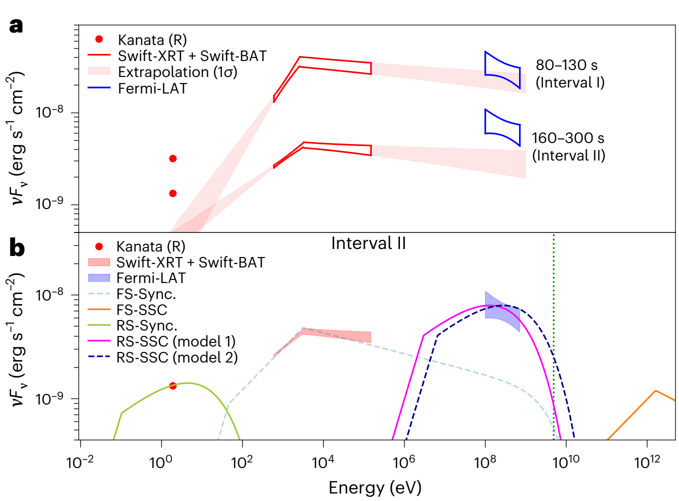

Fig. 3 | SEDs from T_0 + 80 s to T_0 + 300 s and theoretical modelling for time interval II. a,**b**, The red and blue areas correspond to the 1σ confidence regions from the best-fitting functions (that is, a broken power-law function and a simple power-law function, respectively) for the Swift-XRT, Swift-BAT and Fermi-LAT ranges, respectively. The red points represent the optical flux observed by the Kanata telescope. **a**, The pale red shaded regions correspond to the 1σ region extrapolated from the Swift-XRT and Swift-BAT range. **b**, The solid yellow green line represents the synchrotron component from the reverse shock. The solid magenta and the dashed navy lines represent the SSC components from models 1 and 2, respectively (see Methods for more details). The dashed light blue and the solid orange lines represent the synchrotron and SSC components of the forward shock, respectively. The green vertical dotted line corresponds to the highest energy photon of 5 GeV (Supplementary Information). FS, forward shock; RS, reverse shock; sync., synchrotron emission.

at a mean value of ~70°. During $t_{obs} \simeq T_0 + 300$ s to $T_0 + 2{,}000$ s when the light curve undergoes a transition from being reverse shock to forward shock dominated, the PD varies between ~2% and ~8% and the PA changes gradually and continuously. At late times ($t_{obs} \gtrsim T_0 + 5{,}000$ s) when the forward shock dominates the total flux (by a factor of ≥10 at $t_{obs} \simeq T_0 + 10^4$ s, due to the steep temporal index of the reverse shock) as well as the polarized flux, the PD varies between ~0.5% and 2% and the PA shows small fluctuations around its mean value of ~160°. This PA is different from that of the early reverse shock dominated emission by ~90°.

The early ($t_{obs} \lesssim T_0 + 300$ s) ejecta-dominated emission with a relatively high PD and roughly constant PA may originate from a combination of a large-scale, transverse, ordered magnetic field and a random field (for example, from shock microphysical instabilities or turbulence), in which the former dominates the polarized flux and the latter dominates the total flux[19]. The late ($t_{obs} \gtrsim T_0 + 5{,}000$ s) emission is afterglow-dominated not only in terms of the total flux but also in its polarized flux. This is the first measurement of a ~90° difference in PA between the early-time ejecta dominated emission and the late-time shocked external medium emission. It is of great significance as it relates between the magnetic field structures in these two regions and reveals their differences. For example, for the commonly invoked large-scale toroidal magnetic field in the ejecta, which is symmetric around the jet symmetry axis, the early PA would be along the direction from our line of sight (LOS) to the jet axis (Fig. 4). For an afterglow shock-produced magnetic field, the polarization would be in the same direction if it were primarily random in the plane of the shock, as is usually assumed based on theoretical considerations of plasma instabilities[20,21]. However, it may be exactly 90° different from this direction if it is more isotropic just after the shock and then becomes predominantly parallel to the shock normal due to larger stretching along this direction, where the latter dominates the total

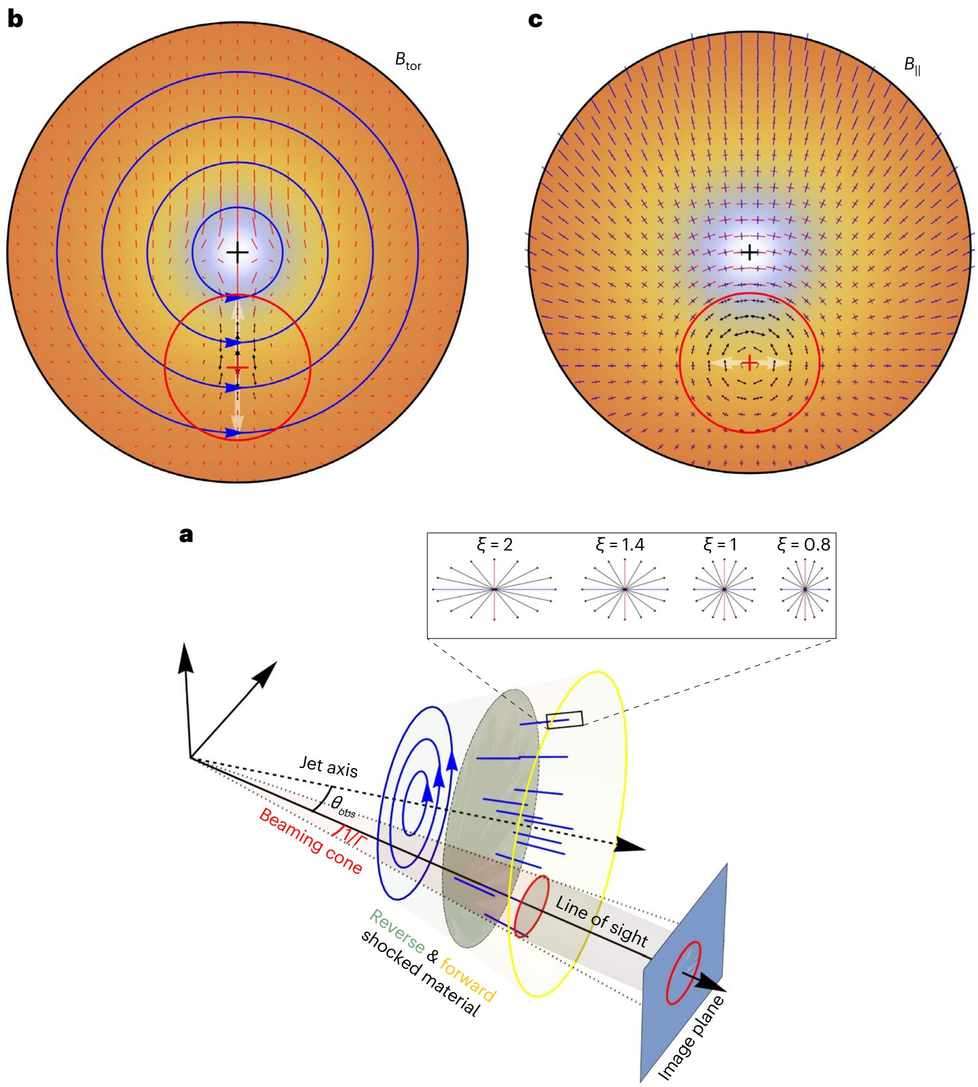

Fig. 4 | Our polarization model. a, The early ($t_{obs} \lesssim T_0 + 300$ s) and late ($t_{obs} \gtrsim T_0 + 5{,}000$ s) flux and polarization are dominated by emission from the reverse- and forward-shock regions, respectively (green and yellow shaded regions). In our model for the measured optical polarization, the reverse-shock region has a large-scale toroidal magnetic field originating from the central source and centred on the jet's symmetry axis (circular blue lines with arrows in **a** and **b**), leading to a relatively large PD of ~1–5%, with the PA along the direction from the LOS (red +) to the jet axis (black +) at early times (**b**). The forward-shock region has a shock-generated magnetic field that is somewhat smaller along the shock normal ($B_{\|}$) than perpendicular to it ($B_{\perp}$). Just behind the shock, $\xi = B_{\|}/B_{\perp} < 1$, but this ratio becomes larger along the shock normal (that is, the radial direction; blue straight lines in **a** and in projection in **c**), so that $\xi > 1$ in most of this region. This occurs since ξ increases with the distance behind the forward shock because of the larger radial stretching of the shocked plasma[19,22] (inset in **a**). This results in a PA perpendicular to the direction from the LOS (red +) to the jet axis (black +), with a relatively small PD $\simeq$ 0.5% to 2% (**c**). **b**, Colour map showing the brighter emission closer to the jet axis, and polarization map for the toroidal magnetic field in the ejecta. The short red lines show the local polarization direction and the double-sided black arrows indicate the local polarized intensity. The red circle around the LOS has angular size $1/\Gamma$, with Γ being the bulk Lorentz factor, and it contains the region dominating the observed flux and polarization. The shaded white double-sided arrow represents the direction and relative strength of the net polarization after averaging over the unresolved GRB image. In addition to the toroidal magnetic field, there is evidence for randomly oriented, small scale, coherent magnetic-field patches (possibly from turbulence or instabilities). These cause large variations in the PD and PA at intermediate times ($t_{obs} \simeq T_0 + 300$ s to $T_0 + 2{,}000$ s) and reduce the otherwise larger degree of polarization at early times. **c**, Polarization map for the radially stretched out, shock-generated, magnetic field (blue field lines in the yellow shaded region in (**a**) that are shown in projection with blue tick marks) behind the forward shock. All else is the same as in (**b**). obs, observed, tor, toroidal.

volume-averaged polarization by a small margin[19,22]. An observation like the one presented here is crucial for distinguishing between these two shock-generated field configurations (shock-normal or shock-plane dominated). At intermediate times ($t_{obs} \simeq T_0 + 300$ s to $T_0 + 2{,}000$ s), the above-described polarizations from the two emission regions nearly cancel each other out, allowing an additional stochastic component to dominate the polarized flux, leading to continuous short-timescale variations of the PA and PD. This stochastic component may arise from turbulent magnetic fields that are coherent on hydrodynamic scales and which can be produced, for example, in shocks[23], by the Richtmyer–Meshkov instability due to density fluctuations[24,25] or by the Rayleigh–Taylor instability at the contact discontinuity[26].

The multi-wavelength observations with polarization measurements of GRB 180720B detected emissions from internal and external forward and reverse shocks, which are major candidates for γ-ray emission regions in GRBs (see Supplementary Information for details for the internal shock). Our results strongly suggest that the early gigaelectronvolt emission is the first robust detection of SSC emission from a reverse shock, which is directly correlated with the optical emission with polarization information, whereas the later teraelectronvolt emission is SSC emission from the forward shock. An SSC origin of early gigaelectronvolt to teraelectronvolt emission may help to resolve the difficulties with a synchrotron origin, namely the violation of the maximum allowed synchrotron photon energy[27–29]. Furthermore, our optical polarization measurements may help to elucidate the origin and structure of GRB magnetic fields, which are tightly coupled to the particle acceleration mechanism.

Methods

Gigaelectronvolt and teraelectronvolt γ-ray observations

Fermi-LAT[30] data were processed with Fermitools 1.2.23, and the event class P8R3_TRANSIENT020E_V2 was used to calculate the γ-ray flux with a power-law function. Here, the radius of the region of interest is 15° and the maximum zenith angle is 100°. The Fermi-LAT observations indicate that the gigaelectronvolt γ-ray emission of this burst lasted for ~1,000 s. The gigaelectronvolt onset time was at T_0 + ~100 s and the gigaelectronvolt flux declined with a temporal index of −1.91 ± 0.31. After T_0 + 900 s, the GRB position was out of the field of view of the LAT with a source off-axis angle of 70°.

The HESS flux area was derived from their observation paper[2], and the effect of the extra-galactic background light was corrected.

X-ray observations

X-ray data from the Swift X-ray Telescope (Swift-XRT) presented in the light curves and spectra in this paper were processed by an automatic analysis procedure[31]. The BAT light curve declined with a temporal index of −1.79 ± 0.02 for T_0 + 20 s to T_0 + 270 s and after that a temporal index of −0.91 ± 0.17. For T_0 + 30 s to T_0 + 270 s, the BAT light curve shows a short variability timescale with $\Delta t < t_{\rm obs}$ and strong spectral evolution, which indicates that the BAT light curve probably originated from an internal shock[32].

The initial bright X-ray flare observed in the XRT data at T_0 + 100 s has rise and decay temporal indices of +4.85 ± 0.44 and −8.18 ± 0.3, respectively, and a hard photon index $\Gamma_{\rm ph}$ = −1.5 ± 0.1 (Fig. 1c). Such a short variability timescale indicates that the X-ray flare did not originate from the afterglow emission site, that is the external shock. Most probably the X-ray flare originated from a different site, for example, an internal shock. The underlying power-law component has temporal indices of −1.22 ± 0.02 (T_0 + 80 s to T_0 + 380 s), −0.75 ± 0.01 (T_0 + 380 s to T_0 + 2,780 s), −1.28 ± 0.02 (T_0 + 2,780 s to T_0 + 1.5 × 10^5 s) and −1.58 ± 0.03 (T_0 + 1.5 × 10^5 s to T_0 + 4.0 × 10^6 s). For T_0 + 380 s to T_0 + 2,780 s, the temporal index is much shallower than a typical one (for example, −1.2), which is called a shallow decay. One of the possible origins is energy injection from a central engine[33,34], which makes the forward-shock emission decay more slowly. Such energy injection may be due to either a long-lived central engine producing a relativistic wind for a long time or a short-lived central engine that produces an outflow with a wide range of Lorentz factors such that slower and more energetic matter resides behind faster-moving matter that eventually catches up with the slower matter and energizes it[34–36].

In the time interval from T_0 + 2,780 s to T_0 + 1.5 × 10^5 s, the observed temporal index of −1.28 ± 0.02 can be interpreted as an normal decay phase in the standard forward-shock afterglow theory[4]. There is a temporal break at T_0 + 1.5 × 10^5 s (±0.2 × 10^5 s), and the difference between the temporal indices is ~0.3. One of the possible break candidates is a cooling break in which the synchrotron cooling frequency passes through the observed frequency. Such a scenario predicts that the photon index becomes softer by 0.5 (ref. 4). However, after T_0 + 1.5 × 10^5 s, the observed photon index ($\Gamma_{\rm ph} \simeq -1.7$) is almost constant as a function of time (Fig. 1b). Thus, the temporal break at T_0 + 1.5 × 10^5 s was not caused by the cooling break but another jet effect (for example, a jet break in which the relativistic jet decelerated and the side expansion became important).

Optical photometric observations

We used optical flux data points obtained by the Kanata and other ground telescopes, as reported in the GCN circulars[3,37–43]. The Kanata observations were performed with the imaging polarimetry mode on the first day (Supplementary Information for Optical polarimetric observations) and with the imaging mode on the second and the third days. All the Kanata photometric data have been calibrated by the relative photometry to nearby stars using the APASS catalogue[44]. Phenomenologically, the optical light curve is represented as a simple power-law component for the reverse shock plus a power-law component with two temporal breaks for the forward shock. For the former power-law component, the best-fitting temporal index is −1.95 ± 0.02. For the latter, the power-law component consists of −0.31 ± 0.01 (before T_0 + 8,300 s), −1.10 ± 0.02 (T_0 + 8,300 s to 1.3 × 10^5 s) and −1.94 ± 0.08 (after T_0 + 1.3 × 10^5 s). For the time interval before T_0 + 8,300 s, the shallow temporal index may indicate that the optical emissions have the same origin as the X-ray emissions in the shallow decay phase described in X-ray observations, but the sparse data points limit any further detailed discussion of this. For T_0 + 8,300 s to 1.3 × 10^5 s, the observed temporal index of −1.10 ± 0.02 is almost the same as the observed X-ray temporal index (−1.28 ± 0.02) in the same time interval. For the time interval after T_0 + 1.3 × 10^5 s, the temporal index is steeper than for the X-rays. The optical temporal break at T_0 + (1.3 ± 0.2) × 10^5 s occurred simultaneously with the X-ray temporal break at T_0 + (1.5 ± 0.2) × 10^5 s, which suggests that the achromatic temporal break at T_0 + ~1.3 × 10^5 s originated from the relativistic effect of the side expansion, which is called a jet break.

SEDs in intervals I and II

For the SEDs from T_0 + 80 s to T_0 + 130 s (interval I) and T_0 + 160 s to T_0 + 300 s (interval II) in which the bright and temporally steep optical and gigaelectronvolt emission was observed, the joint fitting of the Swift-XRT and Swift-BAT data show significantly that the best-fitting function is either the broken power-law function or the Band function rather than the simple power-law function, as shown in Supplementary Table 1. Note that there is no significant difference between the broken power-law function and the Band function. In interval II, the broken power-law function is marginally favoured, so we adopted the broken power-law function to represent the X-ray component in the main text. We also found that using either function does not significantly affect the extrapolation to gigaelectronvolt energies.

For the optical data analysis, we set the extinction of the host galaxy to $A_{\rm v}$ = 0.5 mag as a typical case[45]. The SEDs obtained from the optical band to the gigaelectronvolt band are shown in Fig. 3. In time interval I (T_0 + 80 s to T_0 + 130 s) in which the X-ray flare occurred, the optical component is distinctly higher than the extrapolation from the X-ray component, which is well fitted by the broken power-law function. The excess of the gigaelectronvolt component over the X-ray extrapolation is not significant due to an additional contribution from the X-ray flare probably originating from an internal shock. In time interval II (T_0 + 160 s to T_0 + 300 s), after the occurrence of the X-ray flare, the SED shows that the optical and gigaelectronvolt fluxes are significantly larger than the extrapolations from the best-fitting broken power-law function in the X-ray band (>5σ and ~4σ confidence levels in the optical and gigaelectronvolt bands, respectively). For more details of the gigaelectronvolt excess, see Supplementary Information for Statistical significance of the gigaelectronvolt excess. This indicates that both the optical and gigaelectronvolt components have different origins from the X-ray component. Furthermore, the initial steep temporal index of $\alpha_{\rm opt} \simeq \alpha_{\rm GeV} \simeq -1.9$ suggests that the optical and the gigaelectronvolt components have the same origin, so that the steep temporal index can be interpreted as having a reverse-shock origin[8].

Theoretical modelling of the forward shock in the late afterglow phase (analytical model)

The emission from the forward shock, which is a different emission component from the reverse-shock emission, is not the main topic of this paper. For reference, however, we describe the analytical model for the forward-shock emission. The X-ray light curve, which is dominated by the forward-shock emission, shows complex behaviour, so that it is, unfortunately, hard to reconcile the observed data with a simple model.

To constrain the shock evolution, we first focus on time interval III ($T_0 + 4.5 \times 10^4$ s), in which the very-high-energy γ-ray data was taken with the HESS. In this phase, the emission is dominated by the forward-shock emission. By extracting the SED in time interval IV (Supplementary Fig. 1), we found that the X-ray and optical components are on the same power-law segment with a photon index $\Gamma_{\rm ph} = -1.8$. To explain the observed temporal and spectral indices ($\alpha_{\rm X} \simeq -1.3$ and $\Gamma_{\rm ph} \simeq -1.8$), a circumburst medium with a wind profile ($n(R) \propto R^{-2}$) is in tension with the fast- or slow-cooling synchrotron scenario. Assuming a constant interstellar medium (ISM; $n_{\rm ISM}(R) \propto R^0$), the optical and X-ray temporal decay indices of $\alpha \simeq -1.3$ and the photon spectral index of $\Gamma_{\rm ph} \simeq -1.8$ suggest that the power-law index of the electron injection spectrum is $p \simeq 2.7$. Note that $\alpha = 3(1-p)/4$ and $\Gamma_{\rm ph} = -(1+p)/2$ for $\nu_{\rm m} < \nu_{\rm obs} < \nu_{\rm c}$, where $\nu_{\rm m}$ is the typical synchrotron frequency and $\nu_{\rm c}$ is the synchrotron cooling frequency. The radio flux point suggests that the spectral break at $\nu_{\rm m}$ should exist between the radio and optical bands. The number density of the ISM should be as small as $n_{\rm ISM} \simeq 10^{-3}$ cm^{-3}, because the synchrotron cooling frequency ($\nu_{\rm c} \propto n_{\rm ISM}^{-1}\epsilon_B^{-3/2}$) should be above the XRT band (approximately a few kiloelectronvolts). In addition, ϵ_B is roughly constrained as $\nu_{\rm m}$ ($\propto n_{\rm ISM}^{0}\epsilon_B^{1/2}$) is between the radio and the optical bands (and also for compatibility with the radio flux) and to obtain the correct ratio of the SSC emission to synchrotron emission (Y). Thus, this GRB needs to have an atypically low $n_{\rm ISM}$ of ~10^{-3} cm^{-3}. Such a low $n_{\rm ISM}$ value is not so unlikely and even lower values of ~10^{-4} to 10^{-3} cm^{-3} have been reported for some GRBs with multi-wavelength observations[46,47].

The SSC characteristic frequencies and flux can be derived from the synchrotron ones multiplied by $\gamma_{\rm c}^2$ and the Compton Y parameter, respectively. When the Klein–Nishina effect is neglected[48], $Y = (\epsilon_{\rm e}/\epsilon_B)^{1/2}(\gamma_{\rm c}/\gamma_{\rm m})^{(2-p)/2}$, where $\gamma_{\rm m}$ and $\gamma_{\rm c}$ are the Lorentz factors of minimal energy electrons and those that are cooling at the dynamical time. Following the analytical formulation[49,50], we model the synchrotron and inverse-Compton components at this time interval. Given a snapshot of the spectrum at a certain observation time $t_{\rm obs}$, there are five fitting parameters: the electron spectral index p, the electron minimum Lorentz factor $\gamma_{\rm m}$, the ratio of the energy fractions of non-thermal electrons to the magnetic field $\epsilon_{\rm e}/\epsilon_B$, the magnetic field B and the bulk Lorentz factor $\Gamma_{\rm bulk}$. As summarized in Extended Data Table 1 for $t_{\rm obs} = T_0 + 4.5 \times 10^4$ s, we adopted $\epsilon_{\rm e}/\epsilon_B = 1{,}330$. Taking into account the Klein–Nishina effect, the electron Lorentz factor at the cooling break $\gamma_{\rm c}$ ($>\gamma_{\rm m}$, slow-cooling case) and the Compton Y parameter at $\gamma_{\rm c}$ ($Y_{\rm c}$) are obtained from

$$(1+Y_{\rm c})\gamma_{\rm c} = \frac{6\pi m_{\rm e}c(1+z)}{\sigma_{\rm T}B^2\Gamma_{\rm bulk}t_{\rm obs}}, \quad (1)$$

$$Y_{\rm c}(1+Y_{\rm c}) = \frac{\epsilon_{\rm e}}{\epsilon_{\rm B}}\left(\frac{\gamma_{\rm c}}{\gamma_{\rm m}}\right)^{2-p}\left(\frac{\hat{\gamma}_{\rm c}}{\gamma_{\rm c}}\right)^{(3-p)/2}, \quad (2)$$

where the electron mass $m_{\rm e}$, the speed of light c, the Thomson cross section $\sigma_{\rm T}$ and the Lorentz factor $\hat{\gamma}_{\rm c} \equiv 0.2\Gamma_{\rm bulk}m_{\rm e}c^2/((1+z)h\nu_{\rm c})$ (h is the Planck constant), above which the Klein–Nishina effect prevents electrons from upscattering synchrotron photons at the spectral peak $\nu_{\rm c} \equiv \Gamma_{\rm bulk}\gamma_{\rm c}^2 eB/(2\pi m_{\rm e}c(1+z))$. Our model parameters yield $\gamma_{\rm c} = 1.7 \times 10^6$, $Y_{\rm c} = 2.1$ and $\hat{\gamma}_{\rm c} = 230$. Since $\hat{\gamma}_{\rm c} < \gamma_{\rm m} < \gamma_{\rm c} < \hat{\gamma}_{\rm m} \equiv 0.2\Gamma_{\rm bulk}m_{\rm e}c^2/((1+z)h\nu_{\rm m}) = 2 \times 10^7$, electrons between $\gamma_{\rm m}$ and $\hat{\gamma}_{\rm m}$ can scatter photons with a frequency of $\nu_{\rm m} < \nu < \nu_{\rm c}$. The electron spectrum below $\gamma_{\rm c}$ is $N(\gamma) \propto \gamma^{-p}$ so that the synchrotron spectrum between $\nu_{\rm m} \equiv \Gamma_{\rm bulk}\gamma_{\rm m}^2 eB/(2\pi m_{\rm e}c(1+z))$ and $\nu_{\rm c}$ is $F_\nu \propto \nu^{-(p-1)/2}$. Let us consider that electrons with $\gamma > \gamma_{\rm c}$ cool through SSC emission mainly by scattering target photons with $\nu_{\rm t} \simeq 0.2\Gamma_{\rm bulk}m_{\rm e}c^2/((1+z)h\gamma)$, as the SSC and synchrotron cooling rates are comparable at $\gamma > \gamma_{\rm c}$. In this case, the energy loss rate can be approximated as $\dot{\gamma} \propto \gamma^2\nu_{\rm t}F_{\nu_{\rm t}} \propto \gamma^{(p+1)/2}$. This leads to the electron spectrum above $\gamma_{\rm c}$ as $N(\gamma) \propto \gamma^{-p+1}/\dot{\gamma} \propto \gamma^{-(3p-1)/2}$, which yields the synchrotron spectrum above $\nu_{\rm c}$ as $F_\nu \propto \nu^{-3(p-1)/4}$. The Compton Y parameter decreases with energy as $Y \propto \nu_{\rm t}F_{\nu_{\rm t}} \propto \gamma^{(p-3)/2}$ and $\propto \gamma^{-4/3}$ for $\gamma < \hat{\gamma}_{\rm m}$ and $\gamma > \hat{\gamma}_{\rm m}$, respectively. The synchrotron spectrum should show a structure at $\nu = \nu_0$, as that is the typical synchrotron frequency emitted by electrons with $\gamma = \gamma_0 = 2.6 \times 10^7$ at which $Y = 1$. We omit a detailed discussion about such structures for $\nu = \hat{\nu}_{\rm m}$ or ν_0.

The peak of the SSC spectrum is at $\nu = \nu_{\rm IC} = 2\gamma_{\rm c}\hat{\gamma}_{\rm c}\nu_{\rm c}$, which corresponds to $0.4\gamma_{\rm c}m_{\rm e}c^2$ in the shocked-fluid rest frame. The typical frequency of scattered photons is $\nu \simeq \gamma^2\nu_{\rm t} \propto \gamma$. Then, the SSC spectrum, $F_\nu \propto \gamma N(\gamma)\gamma^2\nu_{\rm t}F_{\nu_{\rm t}}/\nu$ with $\nu_{\rm t} \propto \nu^{-1}$, leads to $F_\nu \propto \nu^{-(p-1)/2}$ and $\propto \nu^{-p+1}$ for $2\gamma_{\rm m}^2\nu_{\rm m} < \nu < \nu_{\rm IC}$ and $\nu > \nu_{\rm IC}$ for inverse-Compton emission, respectively. Our parameter set gives $\nu_{\rm m} = 2.5 \times 10^{13}$ Hz, $\nu_{\rm c} = 2.1 \times 10^{18}$ Hz, $2\gamma_{\rm m}^2\nu_{\rm m} = 1.7 \times 10^{21}$ Hz and $\nu_{\rm IC} = 1.7 \times 10^{27}$ Hz.

The electron energy density obtained from the total energy $(p-1)N_{\rm e}\gamma_{\rm m}m_{\rm e}c^2/(p-2)$ and the volume of the shocked ISM, $\pi R^3/(3\Gamma_{\rm bulk})$, where the radius $R = 4ct_{\rm obs}\Gamma_{\rm bulk}^2/(1+z)$, is equivalent to $(\epsilon_{\rm e}/\epsilon_B)B^2/(8\pi)$, from which the total electron number $N_{\rm e}$ can be written in terms of our five model parameters. The synchrotron flux at $\nu = \nu_{\rm m}$ in this slow-cooling case can be written without an apparent dependence on either the total energy or the ISM density:

$$F_{\nu_{\rm m}} = \Gamma_{\rm bulk}\frac{1+z}{4\pi d_{\rm L}^2}\frac{\sigma_{\rm T}m_{\rm e}c^2B}{3e}N_{\rm e} = \frac{p-2}{p-1}\frac{\epsilon_{\rm e}}{\epsilon_{\rm B}}\frac{2\sigma_{\rm T}c^3t_{\rm obs}^3B^3\Gamma_{\rm bulk}^6}{9\pi(1+z)^2d_{\rm L}^2e\gamma_{\rm m}}, \quad (3)$$

where $d_{\rm L}$ is the luminosity distance and e is the electron charge. Our choice of the parameters gives $\nu_{\rm m}F_{\nu_{\rm m}} = 3.0 \times 10^{-12}$ erg cm^{-2} s^{-1}. Normalized with this value, we plot the model spectrum in Extended Data Fig. 3. The peak ratio of the SSC component to the synchrotron component in the νF_ν plot is given as $Y_{\rm c}$.

From the parameter set, we obtain $\epsilon_{\rm e}/f_{\rm e} = (p-1)\gamma_{\rm m}m_{\rm e}/((p-2)\Gamma_{\rm bulk}m_{\rm p}) = 0.24$ and $\epsilon_B n_{\rm ISM} = B_{\rm f}^2/(32\pi m_{\rm p}c^2\Gamma_{\rm bulk}^2) = 1.1 \times 10^{-6}$ cm^{-3}, where $f_{\rm e}$ is the number fraction of non-thermal electrons and $m_{\rm p}$ is the proton mass. The implied value $f_{\rm e}n_{\rm ISM} = 6.0 \times 10^{-3}$ cm^{-3} suggests a relatively low ISM density. Assuming $\epsilon_{\rm e} = 0.2$, we obtain $\epsilon_B = 1.5 \times 10^{-4}$, $f_{\rm e} = 0.82$ and $n_{\rm ISM} = 7.3 \times 10^{-3}$ cm^{-3}. These values can well reproduce the observed SED in time interval III, as shown in Extended Data Fig. 3. The adopted parameters of the synchrotron shock model (see row 'analytical' in Extended Data Table 1) are mostly consistent with those in previous works for GRB 180720B (ref. 51). The modelled light curves of the forward shock at different frequencies are shown in Extended Data Fig. 1.

Theoretical modelling of the early afterglow with the reverse-shocked component (model 1/2)

In time interval II, the X-ray light curve behaves like that in the typical shallow decay phase, whereas the optical and the gigaelectronvolt γ-ray components decay steeply. First, we model the X-ray component with the forward-shock emission as shown in Fig. 3 ($t_{\rm obs} = T_0 + 200$ s). The model is partially constrained by the spectral model for the time interval III. With the one-zone approximation[52], the flux constrained by equation (3) gives a constant ratio

$$\hat{E} \equiv \frac{E_0}{n_{\rm ISM}} = \frac{4^4\pi m_{\rm p}c^5\Gamma_{\rm bulk}^8}{3(1+z)^3}t_{\rm obs}^3 = 2.3 \times 10^{56}\ {\rm erg\ cm^3}, \quad (4)$$

where E_0 is the total kinetic energy. If we assume a constant $n_{\rm ISM}$, then $\Gamma_{\rm bulk} \simeq 240$ at $t_{\rm obs} = T_0 + 200$ s. However, if we maintain the microscopic parameters adopted for the time interval III ($t_{\rm obs} = T_0 + 4.5 \times 10^4$ s) then the X-ray flux from the forward shock is not reproduced even at $t_{\rm obs} = T_0 + 200$ s. In this period, the X-ray light curve is in the shallow decay phase, but the energy injection model, which implies internal collisions from behind, is not preferable for the steeply decaying reverse-shock emission. The internal collisions should inject energy into the reverse-shocked region too. In addition, the X-ray spectrum shows a break at ~3 keV. If the microscopic parameters are constant, $\nu_{\rm m}$ is still lower than 3 keV, and we obtain $\gamma_{\rm m} \simeq \hat{\gamma}_{\rm m}$, which heavily suppresses the inverse-Compton cooling of electrons above $\gamma_{\rm m}$.

We need a temporal evolution of the microscopic parameters of the forward shock to make a cooling break at ~3 keV. One example of such models is shown in Fig. 3, where the two components, the forward- and reverse-shock components, are shown. Hereafter, we denote the model parameters for the forward (reverse) shock with subscript f (r). For the forward-shock component, we adopt $\Gamma_{\rm bulk,f} = 240$, $p = 2.2$, $\epsilon_{\rm e,f}/\epsilon_{B,\rm f} = 1.33$, $\gamma_{\rm m,f} = 6{,}700$ and $B_{\rm f} = 0.622$ G. The same calculations as those for the late afterglow yield $\hat{\gamma}_{\rm c,f} = 4,700 < \gamma_{\rm c,f} = 5.5\times10^4 < \hat{\gamma}_{\rm m,f} = 3.2\times10^5$, $\nu_{\rm m,f} = 1.1\times10^{16}$ Hz, $\nu_{\rm c,f} = 7.6\times10^{17}$ Hz, $2\gamma_{\rm c,f}\hat{\gamma}_{\rm c,f}\nu_{\rm c,f} = 3.9\times10^{26}$ Hz, $Y_{\rm c,f} = 0.26$ and $\nu_{\rm m,f}F_{\nu_{\rm m,f}} = 8.9\times10^{-10}$ erg cm^{-2} s^{-1}. This parameter set implies that $\epsilon_{\rm e,f}/f_{\rm e,f} = 0.09$ and $\epsilon_{B,\rm f}n_{\rm ISM} = 4.4\times10^{-5}$cm^{-3}. The implied value $f_{\rm e,f}n_{\rm ISM} = 6.5\times10^{-4}$ cm^{-3} with $n_{\rm ISM} = 7.3\times10^{-3}$ cm^{-3} suggests a lower $f_{\rm e}$ (~0.09) compared to the value in interval II and $\epsilon_{\rm e,f} \simeq \epsilon_{B,\rm f} \simeq 10^{-2}$.

Next, we move on to the emission from the shocked ejecta. After the reverse shock crosses the shell, the Blanford–McKee solution[53] is not applicable to the shocked ejecta. A general power-law scaling of $\Gamma_{\rm bulk} \propto R^{-g}$ (ref. 54) is useful for characterizing the evolution of the physical parameters of a reverse shock, where g is a constant in the range $3/2 < g < 7/2$ for the ISM. In this case, the temporal index at the observed band for $\nu_{\rm m,r} < \nu_{\rm obs} < \nu_{\rm c,r}$ is given as $\alpha_{\rm RS}^{\rm syn} = -[(15g+24)p+7g]/(28g+14)$. Adopting $p = 2.35$ and $g = 5/2$, we obtain $\alpha_{\rm RS}^{\rm syn} \approx -1.9$, which is consistent with the observed temporal index of the optical emission. Note that the observed temporal index does not strongly depend on the g index. The temporal index of the SSC emission of the reverse shock is expected to be $\alpha_{\rm RS}^{\rm SSC} = [-3g+26-p(19g+36)]/[14(2g+1)] \approx -2.1$ (ref. 15), and this value is also consistent with the observed temporal index of the gigaelectronvolt γ-ray emission.

Here, we also check whether the temporal index of the LAT emission is compatible with the other model, for example, the SSC component from the forward-shock emission. For $\nu_{\rm m,f}^{\rm SSC} < \nu < \nu_{\rm c,f}^{\rm SSC}$ (or $\nu_{\rm max,f}^{\rm SSC}$) in the slow-cooling regime, the theoretical SSC temporal indices of the forward shock are $(11-9p)/8 \simeq -1.27$ and $-p = -2.35$ in the ISM and wind profiles, respectively, for $p = 2.35$ (refs. 55,56). Since the ISM profile is favoured (Theoretical modelling of the forward shock at the late afterglow phase), the temporal index of the theoretical SSC light curve is inconsistent with the observed temporal index of the LAT light curve (−1.9 ± 0.3). Thus, the scenario that the LAT light curve arises from the forward shock may be rejected. Note that, more conservatively, if we do not determine or constrain the electron index (p) or the external medium density profile, we cannot strongly constrain whether the LAT emission originates from the forward or reverse shock. Thus, temporal information in the gigaelectronvolt band cannot alone put a strong constraint on the emission site. Temporal information from the multi-wavelength observations in the early-to-late phase is crucial.

The optical and γ-ray light curves suggest that the onset of the reverse-shock emissions is earlier than $t_{\rm obs} = T_0 + 100$ s, when $\Gamma_{\rm bulk} \simeq 310$ from equation (4). This is consistent with the deceleration time[52]

$$t_{\rm dec} = \frac{1+z}{2}\left(\frac{3\hat{E}}{32\pi n m_{\rm p} c^5 \Gamma_0^8}\right)^{1/3} \simeq 100\left(\frac{\hat{E}}{2.3\times10^{56}\ {\rm erg\ cm^3}}\right)^{1/3}\left(\frac{\Gamma_0}{310}\right)^{-8/3}\ {\rm s}, \qquad (5)$$

where Γ_0 is the initial Lorentz factor of the ejecta. If the shocked ejecta starts decelerating ($\Gamma_{\rm bulk,r} \propto R^{-5/2} \propto t_{\rm obs}^{-5/12}$) at $t_{\rm obs} = T_0 + 100$ s, we obtain $\Gamma_{\rm bulk,r} = 233$ at $t_{\rm obs} = T_0 + 200$ s. The model parameters constrain the volume of the emission region. The implied width of the shocked region should be comparable to or larger than the typical shell width, $R/(12\Gamma_{\rm bulk,r})$. However, a model with $\Gamma_{\rm bulk,r} \simeq 200$ requires an extremely thin shell. We assume that the optical and γ-ray components are emitted from a slower ejecta, which may correspond to a fraction of the shocked ejecta decelerated by the rarefaction wave. Thus, we adopt $\Gamma_{\rm bulk,r} = 90$ at $t_{\rm obs} = T_0 + 200$ s.

The observed gigaelectronvolt spectrum has a photon index $\Gamma_{\rm ph} = -2.2 \pm 0.2$, which is softer than the theoretical SSC component that has $\Gamma_{\rm ph} = -(1+p)/2 = -1.7$, where $p \simeq 2.35$ as discussed above. This suggests that the SSC component may have a spectral cutoff in the gigaelectronvolt band. Thus, we introduce an additional parameter, the maximum electron Lorentz factor $\gamma_{\rm max,r}$, which may be substantially lower than the values in the forward-shock region. In Fig. 3, we show two models for the reverse-shock emission, which yield the same synchrotron spectrum. Model 1 has a similar $\epsilon_{\rm e}/\epsilon_B$ to the forward-shock region in interval III, whereas we adopt a more extreme value of $\epsilon_{\rm e}/\epsilon_B$ in model 2 to maximize the emission volume. The common parameters are $p = 2.35$ and the maximum Lorentz factor $\gamma_{\rm max,r} = 10\gamma_{\rm m,r}$. Here, the maximum electron energy in the mildly relativistic reverse shock may be different from that in the ultra-relativistic forward shock in GRBs. Recent particle-in-cell simulations[57] produce very soft spectra for electrons accelerated by mildly relativistic shocks, and the spectral softness strongly depends on the magnetic structure. Thus, the efficiency of the injection into the acceleration process in mildly relativistic shocks may be low. Alternatively, the turbulence acceleration rather than the shock acceleration may be the dominant process in the reverse-shock region. Several simulations[58,59] show that the contact discontinuity between the forward and reverse shocks is probably unstable. The turbulence behind the forward shock may destroy the sharp reverse-shock structure.

The other parameters are $\epsilon_{\rm e,r}/\epsilon_{B,\rm r} = 1{,}000$ (3,300), $\gamma_{\rm m,r} = 380$ (565), $B_{\rm r} = 1.1$ G (0.52 G) for model 1 (model 2). The cooling Lorentz factor due to synchrotron radiation is much larger than $\gamma_{\rm max,r}$ as $\gamma_{\rm c,r} = 5.5\times10^4$ and 2.7×10^5 for the models with $\gamma_{\rm m,r} = 380$ and 565, respectively. In these cases, the Klein–Nishina effect is negligible. As the synchrotron cooling time is proportional to γ^{-1}, we can approximate the Compton Y parameter as $Y \simeq \sqrt{\epsilon_{\rm e,r}/\epsilon_{B,\rm r}}(\gamma_{\rm max,r}/\gamma_{\rm m,r})^{(2-p)/2}\sqrt{\gamma_{\rm max,r}/\gamma_{\rm c,r}}$. We have adjusted the parameter $\epsilon_{\rm e,r}/\epsilon_{B,\rm r}$ to the common value $Y = 5.6$ for the two models. The parameter set yields $\nu_{\rm m,r} = 2.5\times10^{13}$ Hz, $\nu_{\rm max,r} = 2.5\times10^{15}$ Hz, $2\gamma_{\rm max,r}^2\nu_{\rm max,r} = 7.2\times10^{22}$ Hz (1.6×10^{23} Hz) for model 1 (model 2), where $\nu_{\rm max}$ is the maximum synchrotron frequency. The spectrum above $\nu_{\rm m}$ is written as $F_\nu \propto \nu^{-(p-1)/2}\exp(-\sqrt{\nu/\nu_{\rm max}})$ Note that on taking into account the gradual cutoff shape above $\nu_{\rm max,r}$ of the SSC emission, the modelled SSC emission from the reverse shock reaches a few gigaelectronvolts, as shown in Fig. 3.

The number of non-thermal electrons $N_{\rm e,r} = f_{\rm e,r}E_{\rm ej}/(\Gamma_0 m_{\rm p}c^2)$, where $E_{\rm ej}$ is the initial total energy of the ejecta before transferring its energy to the forward shock, is constant during the emission. The flux is normalized as

$$\nu_{\rm m,r}F_{\nu_{\rm m,r}} = \frac{1}{4\pi d_{\rm L}^2}\frac{N_{\rm e,r}\sigma_{\rm T}cB_{\rm r}^2\gamma_{\rm m,r}^2\Gamma_{\rm bulk,r}^2}{6\pi} = 7.2\times10^{-10}\ {\rm erg\ cm^{-2}\ s^{-1}}. \qquad (6)$$

Then, we obtain $E_{\rm ej} = 4.0$ (8.7) $\times 10^{53} \times (\Gamma_0/310)\, f_{\rm e,r}^{-1}$ erg for model 1 (model 2). From $V_{\rm r}(\epsilon_{\rm e,r}/\epsilon_{B,\rm r})B_{\rm r}^2/(8\pi) = (p-1)N_{\rm e,r}\gamma_{\rm m,r}m_{\rm e}c^2/(p-2)$, the volume of the emission region is estimated as $V_{\rm r} = 2.0\times10^{49}$ cm^3 (9.4×10^{49}cm^3) for $\gamma_{\rm m,r} = 380$ (565). Since the emission radius is estimated as $R = 4\Gamma_{\rm bulk,r}^2 ct_{\rm obs}/(1+z) = 1.2\times10^{17}$ cm, the shell width in model 1 (model 2) is estimated as 1.1×10^{14} cm (5.4×10^{14} cm), which is close to (larger than) the typical width $R/(12\Gamma_{\rm bulk}) \simeq 1.1\times10^{14}$ cm. The adopted physical parameters used for modelling the reverse-shock afterglow are summarized in Extended Data Table 1 (see row 'model 1/2'). The modelled light curves for the reverse shock at different frequencies are shown in Extended Data Fig. 1. Note that the results of models 1 and 2 are almost identical.

For the maximum SSC photon energy, if inverse-Compton scattering occurs in the Thomson regime, the SSC spectrum extends up to $\gamma_{\rm c,r}^2\nu_{\rm c,r}$. A typical synchrotron cooling energy for a seed photon is $\nu_{\rm c,r} \simeq 1$ keV in the observer frame[8]. Correspondingly, the seed photon energy in the rest frame of the electron is $\nu'_{\rm seed} \approx (1+z)\gamma_{\rm c,r}\nu_{\rm c,r}/\Gamma_{\rm bulk,r} \approx 1$ MeV (~$m_{\rm e}c^2$), where $\nu_{\rm c,r} \simeq 1$ keV, $\gamma_{\rm c,r} \simeq 10^5$ and $\Gamma_{\rm bulk,r} \simeq 90$ are derived from the above model. This GRB has a 5 GeV photon event observed at $T_0 + 142$ s, which was also reported in an earlier work[60]. Although this event is slightly out of the time interval II, the SSC spectrum may be extended to above a few gigaelectronvolt energies, in which case model 2 with the higher-energy emission may be favoured over model 1. The high-energy cutoff of the SSC emission from the reverse shock $\nu^{\rm SSC}_{\rm cutoff,r}$ is determined by $\gamma_{\rm max,r}$. Thus, if we slightly modify $\gamma_{\rm max,r}$, the cutoff energy can be extended to higher energies ($\nu^{\rm SSC}_{\rm cutoff,r} \propto \gamma^2_{\rm max,r}$). The Klein–Nishina effect can strongly affect SSC photons on the high-energy side, and the highest photon energy of the SSC component could be limited to $\Gamma_{\rm bulk,r}(1+z)^{-1}\gamma_{\rm c,r}m_{\rm e}c^2 \simeq 10(1+z)^{-1}$ TeV, which is larger than the LAT energy range. Note that the seed photon energy for the second-order inverse-Compton emission in the rest frame of the electron is $\nu'_{\rm seed,SSC} \approx (1+z)\gamma_{\rm m,r}\nu_{\rm SSC,1st}/\Gamma_{\rm bulk,r} \approx 700$ MeV, which is larger than the electron rest mass energy $m_{\rm e}c^2$. At these energies, the scattering cross section is highly suppressed, and therefore, we ignore the second-order inverse-Compton emission for this GRB. To realize the maximum SSC photon or spectral cutoff at gigaelectronvolt energies, the maximum accelerated electron energy ($\gamma_{\rm max,r}$) of the reverse-shock synchrotron component should be lower than $\gamma_{\rm c,r}$ (for example, $\gamma_{\rm max,r} \simeq 5\times10^3 \simeq 3m_{\rm p}/m_{\rm e}$).

Thus, for GRB 180720B, we see possible evidence for a spectral cutoff, but this cutoff depends sensitively on the acceleration mechanism for the reverse shock, which originates from GRB ejecta and is characterized by the nature of the GRB central engine, for example, the initial strong magnetic field around the black hole[61,62].

Previous works investigated the low synchrotron optical flux from the reverse shock in GRBs while assuming a high magnetization in the GRB ejecta[63]. As seen for this GRB, a high Y value can suppress the synchrotron optical flux from the reverse shock without assuming a high magnetization. Thus, few previous works constrained the Y value directly due to a lack of simultaneous observations of the synchrotron and SSC components from the reverse shock. Our findings have important implications for understanding the physical mechanism of a reverse shock.

Theoretical modelling of the afterglow with the time-independent parameters (EATS model)

We also tested the theoretical model with the time-independent shock microphysical parameters to reproduce the afterglow emission in the early and late phases (intervals II and III). This model[64] calculates the observed flux at any given observer's time $T_{\rm obs}$ by integrating over the equal arrival time surface (EATS) of the GRB jet, which includes contributions from the emission arising from shocked gas within the beaming cone (of angular size $1/\Gamma_{\rm bulk}$; Fig. 4a) centred at the observer's LOS. An EATS integration then properly accounts for the simultaneous arrival time of photons that were emitted at an earlier central-engine-frame time by material at a small angular distance away from the LOS and those emitted by the shocked gas along the LOS but at a later central-engine-frame time. Thus, this model describes the realistic flux and spectral evolution of the afterglow emission.

By adopting the parameters in Extended Data Table 1 (see row 'EATS'), the model can reproduce the observed multi-wavelength data at time intervals II and III with the time-independent parameters (Extended Data Fig. 2). Note that $\gamma_{\rm m}$ and $\gamma_{\rm c}$ are not shown in Extended Data Table 1 because those values are continuous for the EATS model and a single value cannot easily be defined.

By reproducing the LAT light curve, this model clearly demonstrates that the origin of the LAT gigaelectronvolt flux is SSC emission from the reverse shock. A jet break is not added to the EATS model to reproduce the X-ray light curve in the late phase. This model deviates from the radio data. A similar difficulty in reproducing the radio observations was reported in a multi-wavelength study from the radio to the teraelectronvolt band[29]. One of the important features of the EATS model is that the synchrotron emission from the reverse shock extends well into the X-ray band, which is different from the analytical model, which includes only photons emitted along the LOS. At the time of interval II, the X-ray band is above the cutoff frequency (above which the shocked plasma cannot radiate after the reverse-shock crossing) for radiation emitted along the LOS. Therefore, the flux contribution to the X-ray band comes only from radiation emitted from small angles away from the LOS and at earlier laboratory-frame times when the cutoff frequency was still above the X-ray band. For this reason, the detailed spectral modelling with EATS integration is important. Earlier analytical works may not have considered this effect.

This model gives a very low value of $\epsilon_{B,f}$ (~10^{-4}) in the early phase, which induces the strong SSC component in the teraelectronvolt band and may cause secondary cascade emission and contribute to the gigaelectronvolt band. To check whether the teraelectronvolt emission induces the secondary cascade emission, we calculated the opacity of the teraelectronvolt emission. First, the teraelectronvolt photons with $E_{\rm TeV} \simeq 10^{12}$ eV mainly interact with target photons with energy $E_{\rm t} = (m_{\rm e}c^2)^2\Gamma^2_{\rm bulk}E^{-1}_{\rm TeV}(1+z)^{-2} \approx 10\ {\rm keV}\ \ (\Gamma_{\rm bulk}/300)^2(E_{\rm TeV}/1\,{\rm TeV})^{-1}$. The target photon flux at $E_{\rm t} \simeq 10$ keV is roughly $F_{\rm t} \simeq 5\times10^{-9}$ erg cm^{-2} s^{-1}, that is, the target photon luminosity $L_{\rm t} = 4\pi d_{\rm L}^2F_{\rm t} \approx 10^{49}$ erg s^{-1}, where $d_{\rm L}$ is the luminosity distance of 4.0 Gpc. Thus, the target photon density $n_{\rm t}$ can be obtained as $L_{\rm t}/4\pi R^2\Gamma_{\rm bulk}cE_{\rm t}$, where R is the radius of the GRB ejecta and $R \approx 4c\Gamma^2_{\rm bulk}t_{\rm obs}(1+z)^{-1} \approx 10^{18}$ cm, where c is the speed of light. Then, we calculate the opacity of the teraelectronvolt emission in the GRB emission site as $\tau = n_{\rm t}\sigma_{\gamma\gamma}R/\Gamma_{\rm bulk} \simeq 10^{-3}$, where $\sigma_{\gamma\gamma}$ is the cross section of the γ–γ annihilation and is roughly ~$0.1\sigma_{\rm T}$, where $\sigma_{\rm T}$ is the Thomson cross section. This result indicates that the teraelectronvolt emission is optically thin and that the secondary cascade emission does not occur from the strong SSC photons. When calculating the model spectrum, only synchrotron photons from the forward-shock region were considered as target photons for inverse-Compton scattering. However, if photons below 100 eV originating from the reverse-shock region also contributed as inverse-Compton seed photons, then the inverse-Compton component should have a low-energy tail, whose flux can potentially exceed the observed gigaelectronvolt flux in interval II. (This requires further more detailed investigation that is outside the scope of this work.) We note this weakness in such a high Compton Y model in the early phase.

Do the early optical and gigaelectronvolt emissions arise from the tail of the prompt emission?

Figure 1 shows that the light curves at all frequencies appear to be decaying at a consistent rate for the first few hundred seconds. They may have the same origin, such as the tail of the prompt emission[65]. One of the strong pieces of evidence for the tail of the prompt emission is the spectral softening with time, which has been observed for Swift GRBs[66] and can be interpreted as the curvature effect of a spherical, relativistic jet[67,68]. For the XRT and BAT data for this GRB, the significant spectral softening was observed, as seen in the photon index evolution of Fig. 1, which implies that the early emission may arise from the tail of the prompt emission. For some previous LAT GRBs, spectral softening was observed[69], which can be also interpreted as the tail of the prompt emission. However, in the LAT light curve of this GRB, no such spectral softening was seen in the first few hundred seconds. Instead, the photon index remained almost flat.

For the optical data, the spectral evolution cannot be observed due to photometry in a single band. Here, if the early optical and gigaelectronvolt emissions originated from the tail of the prompt emission, they should dominate the other component. That is, the observed SED could be represented by a single component such as a synchrotron model[70]. However, the observed SED indicates that there are several components in interval II. Note that although the prompt optical emission for several GRBs has a different spectral component from the X-ray and gamma-ray emission[71,72], the observed temporal indices of the prompt optical emission (for example, approximately −7 and approximately −14 for GRBs 080319B and 160625B, respectively) are much steeper than that of this GRB. Thus, the observed spectral and temporal properties in the optical and gigaelectronvolt bands disfavour the scenario of the tail of the prompt emission for this GRB.

Data availability

The Fermi-LAT data are publicly available at the Fermi Science Support Center website: https://fermi.gsfc.nasa.gov/ssc/. Swift-XRT and BAT products are available from the online GRB repository https://www.swift.ac.uk/xrt_products. All the raw data from HOWPol and HONIR can be downloaded from the SMOKA data archiving site within the website of the National Astronomical Observatory of Japan: https://smoka.nao.ac.jp/index.jsp. The processed data are available from the corresponding author upon request.

Code availability

The details of the code are fully described in Methods. Code that can reproduce each figure in the paper is available from the corresponding author upon request.

References

1. Vreeswijk, P. M. et al. GRB 180720B: VLT/X-shooter redshift. *GRB Coord. Netw.* **22996**, 1 (2018).
2. Abdalla, H. et al. A very-high-energy component deep in the γ-ray burst afterglow. *Nature* **575**, 464–467 (2019).
3. Sasada, M. et al. GRB 180720B: Kanata 1.5 m optical/NIR observation. *GRB Coord. Netw.* **22977**, 1 (2018).
4. Sari, R., Piran, T. & Narayan, R. Spectra and light curves of gamma-ray burst afterglows. *Astrophys. J. Lett.* **497**, L17–L20 (1998).
5. Ajello, M. et al. A decade of gamma-ray bursts observed by Fermi-LAT: the second GRB catalog. *Astrophys. J.* **878**, 52 (2019).
6. Mundell, C. G. et al. Highly polarized light from stable ordered magnetic fields in GRB 120308A. *Nature* **504**, 119–121 (2013).
7. Sari, R. & Piran, T. Hydrodynamic timescales and temporal structure of gamma-ray bursts. *Astrophys. J. Lett.* **455**, L143 (1995).
8. Kobayashi, S. Light curves of gamma-ray burst optical flashes. *Astrophys. J.* **545**, 807–812 (2000).
9. Wang, X. Y., Dai, Z. G. & Lu, T. Prompt high-energy gamma-ray emission from the synchrotron self-Compton process in the reverse shocks of gamma-ray bursts. *Astrophys. J. Lett.* **546**, L33–L37 (2001).
10. Wang, X. Y., Dai, Z. G. & Lu, T. The inverse Compton emission spectra in the very early afterglows of gamma-ray bursts. *Astrophys. J.* **556**, 1010–1016 (2001).
11. Zhang, B. & Mészáros, P. High-energy spectral components in gamma-ray burst afterglows. *Astrophys. J.* **559**, 110–122 (2001).
12. Fraija, N., Lee, W. & Veres, P. Modeling the early multiwavelength emission in GRB130427A. *Astrophys. J.* **818**, 190 (2016).
13. Fraija, N. et al. Theoretical description of GRB 160625B with wind-to-ISM transition and implications for a magnetized outflow. *Astrophys. J.* **848**, 15 (2017).
14. Fraija, N. et al. Analysis and modeling of the multi-wavelength observations of the luminous GRB 190114C. *Astrophys. J. Lett.* **879**, L26 (2019).
15. Fraija, N. et al. GRB Fermi-LAT afterglows: explaining flares, breaks, and energetic photons. *Astrophys. J.* **905**, 112 (2020).
16. Zhang, B. T. et al. External inverse-Compton and proton synchrotron emission from the reverse shock as the origin of VHE gamma rays from the hyper-bright GRB 221009A. *Astrophys. J. Lett.* **947**, L14 (2023).
17. Cherenkov Telescope Array Consortium et al.Science with the Cherenkov Telescope Array. *Astrophys. J. Suppl.* **240**, 32 (2019).
18. Harrison, R. & Kobayashi, S. Magnetization degree of gamma-ray burst fireballs: numerical study. *Astrophys. J.* **772**, 101 (2013).
19. Granot, J. & Königl, A. Linear polarization in gamma-ray bursts: the case for an ordered magnetic field. *Astrophys. J. Lett.* **594**, L83–L87 (2003).
20. Medvedev, M. V. & Loeb, A. Generation of magnetic fields in the relativistic shock of gamma-ray burst sources. *Astrophys. J.* **526**, 697–706 (1999).
21. Keshet, U., Katz, B., Spitkovsky, A. & Waxman, E. Magnetic field evolution in relativistic unmagnetized collisionless shocks. *Astrophys. J. Lett.* **693**, L127–L130 (2009).
22. Gill, R. & Granot, J. Constraining the magnetic field structure in collisionless relativistic shocks with a radio afterglow polarization upper limit in GW 170817. *Mon. Not. R. Astron. Soc.* **491**, 5815–5825 (2020).
23. Gruzinov, A. & Waxman, E. Gamma-ray burst afterglow: polarization and analytic light curves. *Astrophys. J.* **511**, 852–861 (1999).
24. Sironi, L. & Goodman, J. Production of magnetic energy by macroscopic turbulence in GRB afterglows. *Astrophys. J.* **671**, 1858–1867 (2007).
25. Inoue, T., Asano, K. & Ioka, K. Three-dimensional simulations of magnetohydrodynamic turbulence behind relativistic shock waves and their implications for gamma-ray bursts. *Astrophys. J.* **734**, 77 (2011).
26. Duffell, P. C. & MacFadyen, A. I. Shock corrugation by Rayleigh–Taylor instability in gamma-ray burst afterglow jets. *Astrophys. J. Lett.* **791**, L1 (2014).
27. Ackermann, M. et al. Fermi-LAT observations of the gamma-ray burst GRB 130427A. *Science* **343**, 42–47 (2014).
28. MAGIC Collaboration. Teraelectronvolt emission from the γ-ray burst GRB 190114C. *Nature* **575**, 455–458 (2019).
29. MAGIC Collaboration. Observation of inverse Compton emission from a long γ-ray burst. *Nature* **575**, 459–463 (2019).
30. Atwood, W. B. et al. The Large Area Telescope on the Fermi Gamma-Ray Space Telescope Mission. *Astrophys. J.* **697**, 1071–1102 (2009).
31. Evans, P. A. et al. Methods and results of an automatic analysis of a complete sample of Swift-XRT observations of GRBs. *Mon. Not. R. Astron. Soc.* **397**, 1177–1201 (2009).
32. Falcone, A. D. et al. The giant X-ray flare of GRB 050502B: evidence for late-time internal engine activity. *Astrophys. J.* **641**, 1010–1017 (2006).
33. Nousek, J. A. et al. Evidence for a canonical gamma-ray burst afterglow light curve in the Swift XRT data. *Astrophys. J.* **642**, 389–400 (2006).
34. Zhang, B. et al. Physical processes shaping gamma-ray burst X-ray afterglow light curves: theoretical implications from the Swift X-ray telescope observations. *Astrophys. J.* **642**, 354–370 (2006).
35. Rees, M. J. & Mészáros, P. Refreshed shocks and afterglow longevity in gamma-ray bursts. *Astrophys. J. Lett.* **496**, L1–L4 (1998).
36. Melandri, A. et al. Evidence for energy injection and a fine-tuned central engine at optical wavelengths in GRB 070419A. *Mon. Not. R. Astron. Soc.* **395**, 1941–1949 (2009).
37. Reva, I. et al. GRB 180720B : TSHAO optical observations. *GRB Coord. Netw.* **22979**, 1 (2018).
38. Itoh, R. et al. GRB 180720B: MITSuME Akeno optical observations. *GRB Coord. Netw.* **22983**, 1 (2018).
39. Kann, D. A., Izzo, L. & Casanova, V. GRB 180720B: OSN detection, fading. *GRB Coord. Netw.* **22985**, 1 (2018).
40. Crouzet, N. & Malesani, D. B. GRB 180720B: LCO optical afterglow observations. *GRB Coord. Netw.* **22988**, 1 (2018).
41. Horiuchi, T. et al. GRB 180720B: MITSuME Ishigaki optical observations. *GRB Coord. Netw.* **23004**, 1 (2018).
42. Schmalz, S. et al. GRB 180720B: ISON-Castelgrande optical observations. *GRB Coord. Netw.* **23020**, 1 (2018).
43. Zheng, W. & Filippenko, A. V. GRB 180720B: KAIT optical observations. *GRB Coord. Netw/* **23033**, 1 (2018).
44. Henden, A. A. et al. VizieR online data catalog: AAVSO photometric all sky survey (APASS) DR9 (Henden+, 2016). *VizieR Online Data Catalog* II–336 (2016).

45. Schady, P. et al. The dust extinction curves of gamma-ray burst host galaxies. *Astron. Astrophys.* **537**, A15 (2012).
46. Laskar, T. et al. Energy injection in gamma-ray burst afterglows. *Astrophys. J.* **814**, 1 (2015).
47. Laskar, T. et al. First ALMA light curve constrains refreshed reverse shocks and jet magnetization in GRB 161219B. *Astrophys. J.* **862**, 94 (2018).
48. Sari, R. & Esin, A. A. On the synchrotron self-Compton emission from relativistic shocks and its implications for gamma-ray burst afterglows. *Astrophys. J.* **548**, 787–799 (2001).
49. Nakar, E., Ando, S. & Sari, R. Klein–Nishina effects on optically thin synchrotron and synchrotron self-Compton spectrum. *Astrophys. J.* **703**, 675–691 (2009).
50. Yamasaki, S. & Piran, T. Analytic modeling of synchrotron-self-Compton spectra: application to GRB 190114C. *Mon. Not. R. Astron. Soc.* **512**, 2142–2153 (2022).
51. Wang, X.-Y., Liu, R.-Y., Zhang, H.-M., Xi, S.-Q. & Zhang, B. Synchrotron self-Compton emission from external shocks as the origin of the sub-TeV emission in GRB 180720B and GRB 190114C. *Astrophys. J.* **884**, 117 (2019).
52. Fukushima, T., To, S., Asano, K. & Fujita, Y. Temporal evolution of the gamma-ray burst afterglow spectrum for an observer: GeV–TeV synchrotron self-Compton light curve. *Astrophys. J.* **844**, 92 (2017).
53. Blandford, R. D. & McKee, C. F. Fluid dynamics of relativistic blast waves. *Phys. Fluids* **19**, 1130–1138 (1976).
54. Kobayashi, S. & Sari, R. Optical flashes and radio flares in gamma-ray burst afterglow: numerical study. *Astrophys. J.* **542**, 819–828 (2000).
55. Panaitescu, A. & Kumar, P. Analytic light curves of gamma-ray burst afterglows: homogeneous versus wind external media. *Astrophys. J.* **543**, 66–76 (2000).
56. Fraija, N., Barniol Duran, R., Dichiara, S. & Beniamini, P. Synchrotron self-Compton as a likely mechanism of photons beyond the synchrotron limit in GRB 190114C. *Astrophys. J.* **883**, 162 (2019).
57. Rassel, M. et al. Particle in cell simulations of mildly relativistic outflows in kilonova emissions. *Astrophys. J.* **952**, 165 (2023).
58. Duffell, P. C. & MacFadyen, A. I. Rayleigh–Taylor instability in a relativistic fireball on a moving computational grid. *Astrophys. J.* **775**, 87 (2013).
59. Vanthieghem, A. et al. Physics and phenomenology of weakly magnetized, relativistic astrophysical shock waves. *Galaxies* **8**, 33 (2020).
60. Fraija, N. et al. Modeling the observations of GRB 180720B: from radio to sub-TeV gamma-rays. *Astrophys. J.* **885**, 29 (2019).
61. Mészáros, P. & Rees, M. J. Poynting jets from black holes and cosmological gamma-ray bursts. *Astrophys. J. Lett.* **482**, L29–L32 (1997).
62. Komissarov, S. S. & Barkov, M. V. Activation of the Blandford–Znajek mechanism in collapsing stars. *Mon. Not. R. Astron. Soc.* **397**, 1153–1168 (2009).
63. Jin, Z. P. & Fan, Y. Z. GRB 060418 and 060607A: the medium surrounding the progenitor and the weak reverse shock emission. *Mon. Not. R. Astron. Soc.* **378**, 1043–1048 (2007).
64. Gill, R. & Granot, J. Afterglow imaging and polarization of misaligned structured GRB jets and cocoons: breaking the degeneracy in GRB 170817A. *Mon. Not. R. Astron. Soc.* **478**, 4128–4141 (2018).
65. Tagliaferri, G. et al. An unexpectedly rapid decline in the X-ray afterglow emission of long γ-ray bursts. *Nature* **436**, 985–988 (2005).
66. Zhang, B.-B., Liang, E.-W. & Zhang, B. A comprehensive analysis of Swift XRT data. I. Apparent spectral evolution of gamma-ray burst X-ray tails. *Astrophys. J.* **666**, 1002–1011 (2007).
67. Kumar, P. & Panaitescu, A. Afterglow emission from naked gamma-ray bursts. *Astrophys. J. Lett.* **541**, L51–L54 (2000).
68. Toma, K., Ioka, K., Sakamoto, T. & Nakamura, T. Low-luminosity GRB 060218: a collapsar jet from a neutron star, leaving a magnetar as a remnant? *Astrophys. J.* **659**, 1420–1430 (2007).
69. Ajello, M. et al. Bright gamma-ray flares observed in GRB 131108A. *Astrophys. J. Lett.* **886**, L33 (2019).
70. Oganesyan, G., Nava, L., Ghirlanda, G., Melandri, A. & Celotti, A. Prompt optical emission as a signature of synchrotron radiation in gamma-ray bursts. *Astron. Astrophys.* **628**, A59 (2019).
71. Racusin, J. L. et al. Broadband observations of the naked-eye γ-ray burst GRB080319B. *Nature* **455**, 183–188 (2008).
72. Lü, H.-J. et al. Extremely bright GRB 160625B with multiple emission episodes: evidence for long-term ejecta evolution. *Astrophys. J.* **849**, 71 (2017).

Acknowledgements

The Fermi-LAT Collaboration acknowledges support for LAT development, operation and data analysis from NASA and the Department of the Energy (DOE) (United States); the Institute of Research into the Fundamental Laws of the Universe within the French Alternative Energies and Atomic Energy Commission and Institut national de physique nucléaire et de physique des particules within the French National Centre for Scientific Research (France); the Italian Space Agency and Istituto Nazionale di Fisica Nucleare (Italy); the Ministry of Education, Culture, Sports, Science and Technology (MEXT), the High Energy Accelerator Research Organization and the Japan Aerospace Exploration Agency (Japan); and the K.A. Wallenberg Foundation, the Swedish Research Council and the National Space Board (Sweden). Science analysis support in the operations phase from the National Institute for Astrophysics (Italy) and the National Centre for Space Studies (France) is also gratefully acknowledged. This work was performed in part under DOE Contract DE-AC02-76SF00515 and was supported by MEXT and the Japan Society for the Promotion of Science (JSPS) (KAKENHI Grant Nos. JP17H06362 and JP23H04898), the JSPS Leading Initiative for Excellent Young Researchers programme and the CHOZEN Project of Kanazawa University (M.A.). R.G. acknowledges financial support from the UNAM-DGAPA-PAPIIT IA105823 grant (Mexico). J.G. acknowledges financial support from a joint research programme of the Natural Science Foundation of China and the Israel Science Foundation (Grant No. 3296/19).

Author contributions

M.A. contributed to the analysis of the X-ray and gigaelectronvolt data, the interpretation and the writing of the manuscript. K.A., K. Toma, R.G. and J.G. provided the interpretation and contributed to the writing of the paper. S.R. contributed to the interpretation of the GRB model. K.K., K.N., T.N., K. Takagi, M.K., M.Y. and M.S. contributed to the optical Kanata observations and the optical data analysis. M.O., S.T., N.O. and H.G. analysed the X-ray and gigaelectronvolt data. All authors reviewed the manuscript.

Competing interests

The authors declare no competing interests.

Additional information

Extended data Extended data are available for this paper at https://doi.org/10.1038/s41550-023-02119-1.

Supplementary information The online version contains supplementary material available at https://doi.org/10.1038/s41550-023-02119-1.

Correspondence and requests for materials should be addressed to Makoto Arimoto.

https://doi.org/10.1038/s41550-023-02119-1

Peer review information *Nature Astronomy* thanks Nissim Fraija and the other, anonymous, reviewer(s) for their contribution to the peer review of this work.

Reprints and permissions information is available at www.nature.com/reprints.

Publisher's note Springer Nature remains neutral with regard to jurisdictional claims in published maps and institutional affiliations.

[1]Institute of Science and Engineering, Kanazawa University, Kanazawa, Japan. [2]Institute for Cosmic Ray Research, The University of Tokyo, Kashiwa, Japan. [3]Hiroshima Astrophysical Science Center, Hiroshima University, Higashi-Hiroshima, Japan. [4]Department of Physical Science, Hiroshima University, Higashi-Hiroshima, Japan. [5]Frontier Research Institute for Interdisciplinary Sciences, Tohoku University, Sendai, Japan. [6]Graduate School of Science, Tohoku University, Sendai, Japan. [7]Instituto de Radioastronomía y Astrofísica, Universidad Nacional Autónoma de México, Morelia, Mexico. [8]Astrophysics Research Center of the Open university (ARCO), The Open University of Israel, Ra'anana, Israel. [9]Department of Natural Sciences, The Open University of Israel, Ra'anana, Israel. [10]Department of Physics, The George Washington University, Washington, DC, USA. [11]Nishi-Harima Astronomical Observatory, Center for Astronomy, University of Hyogo, Sayo, Japan. [12]Amanogawa Galaxy Astronomy Research Center, Kagoshima University, Kagoshima, Japan. [13]Department of Physics, Tokyo Institute of Technology, Tokyo, Japan. [14]Centre for Astro-Particle Physics (CAPP) and Department of Physics, University of Johannesburg, Auckland Park, South Africa. ✉e-mail: arimoto@se.kanazawa-u.ac.jp

 https://doi.org/10.1038/s41550-023-02119-1

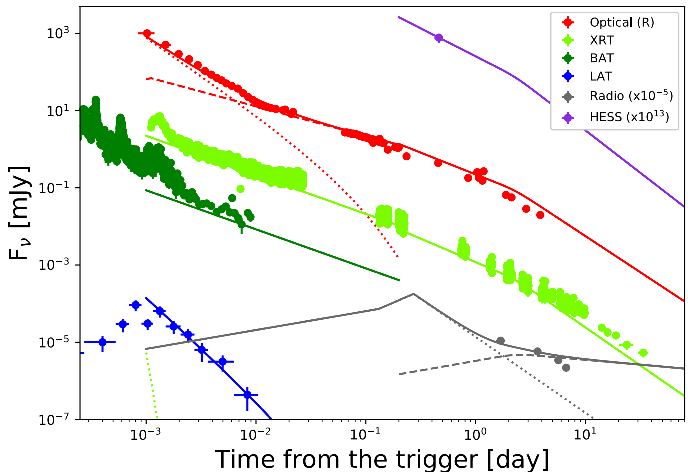

Extended Data Fig. 1 | Lightcurves of the afterglow with the analytical model. The observed flux density lightcurves at different frequencies (Fermi-LAT at 300 MeV, HESS at 300 GeV, optical at 4.6×10^{14} Hz, Swift-XRT at 2 keV, Swift-BAT at 30 keV, and radio at 15.5 GHz) are shown along with the theoretical reverse-shock (dotted), forward-shock (dashed) and combined reverse-shock plus forward-shock (solid) components. Note that the reverse-shock emission in the XRT band is suppressed because the maximum synchrotron frequency is much lower than the X-ray band. Errors correspond to the 1-σ confidence region.

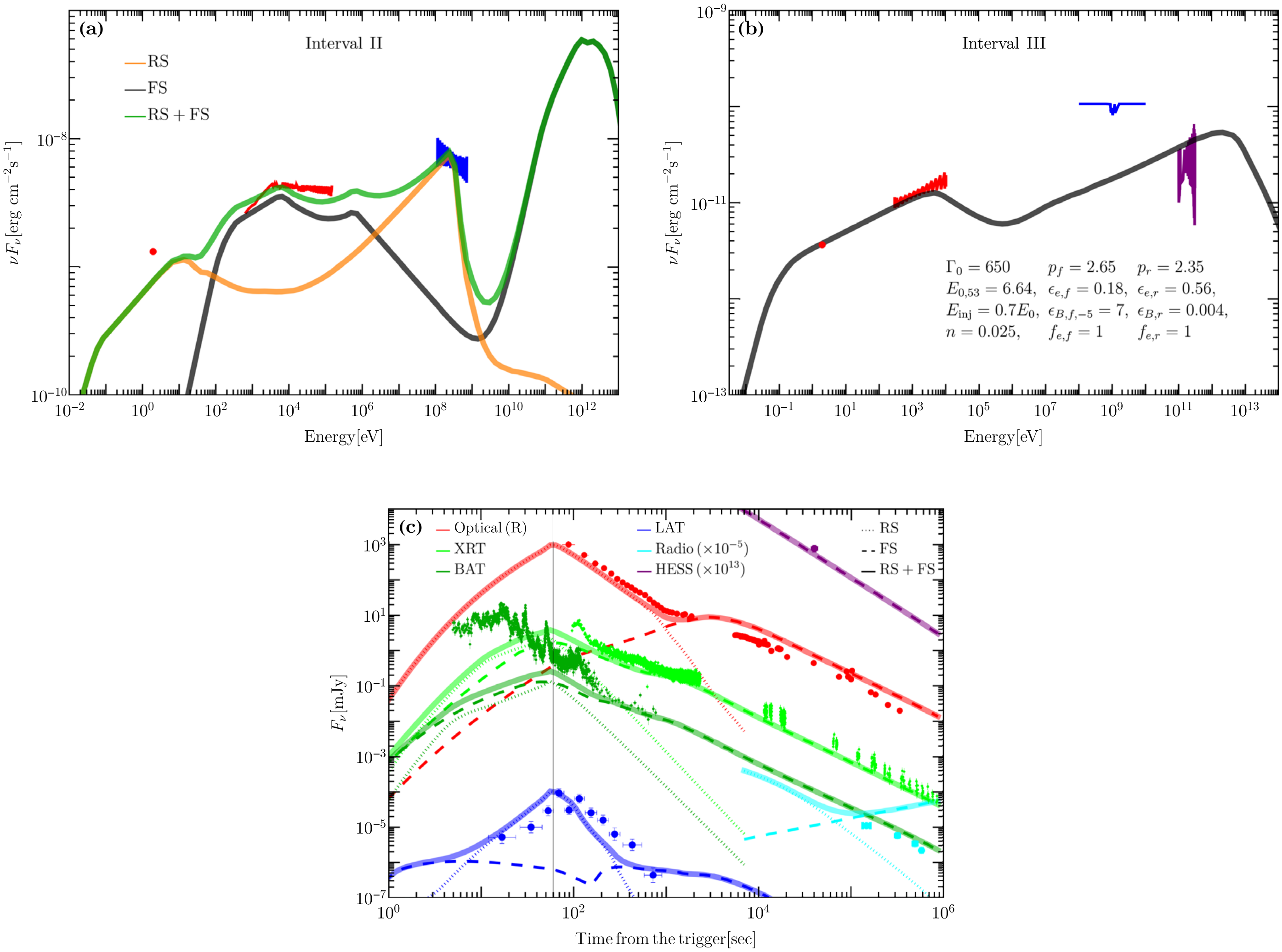

Extended Data Fig. 2 | Theoretical model with time-independent parameters at time intervals II and III. (**a**) Spectral energy distribution at time interval II with the EATS model. The reverse- (RS) and forward-shock (FS) components are shown with the synchrotron and SSC emission. (**b**) Spectral energy distribution at time interval III with the EATS model. The legend shows the adopted model parameters. Here Γ_0 is the bulk Lorentz factor of the coasting flow before it is decelerated by the ISM, E_{inj} is the amount of energy injected during the shallow plateau phase, and subscripts '*f*' and '*r*' refer to FS and RS parameters, respectively. (**c**) Multi-waveband lightcurve and model comparison. The vertical line shows the duration of the prompt GRB. See the caption of Extended Data Fig. 1 for details. Errors correspond to the 1-σ confidence region.

https://doi.org/10.1038/s41550-023-02119-1

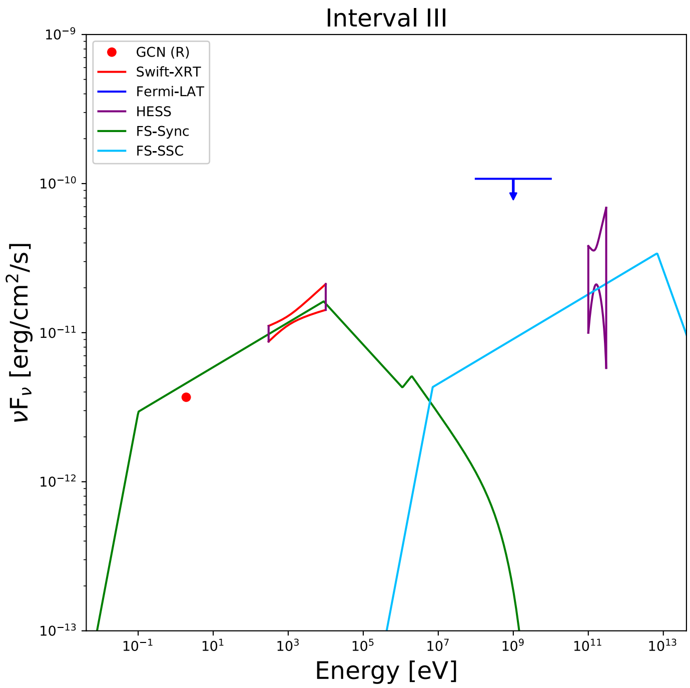

Extended Data Fig. 3 | Spectral energy distribution at time interval III. The solid lines in the low-energy and high-energy bands represent the synchrotron and SSC components from the forward shock with the "analytical" model, respectively. The red area corresponds to the 1-σ confidence region from the best-fit power-law function for the Swift-XRT. Note that the XRT observation was not actually performed in the time interval and we used the interpolated flux before and after the interval (this interpolation is reasonable because the photon index is almost constant from $T_0 + 10^4$ s to 10^5 s, as shown in the bottom panel of Fig. 1. The blue arrow represents the 90% upper limit in the Fermi-LAT range. The red point represents the optical flux observed by the optical telescope. The purple area represents the 1-σ confidence region from the best-fit power-law function for the HESS.

 https://doi.org/10.1038/s41550-023-02119-1

Extended Data Table 1 | Model parameters used for reverse and forward shocks afterglow modeling and output parameters

	t_{obs} [s]	Γ_{bulk}	p	B [G]	ϵ_{e}	ϵ_B	γ_{m}	γ_{c}	f_{e}	n_{ISM} [cm^{-3}]	E_{tot} [erg]
FS "model 1/2"	200	240	2.2	0.622	8×10^{-3}	6×10^{-3}	6.7×10^{3}	5.5×10^{4}	0.088	7.3×10^{-3}	1.6×10^{54}
FS "analytical"	4.5×10^{4}	32	2.7	0.013	0.2	1.5×10^{-4}	5.9×10^{3}	1.7×10^{6}	0.82	7.3×10^{-3}	1.6×10^{54}
FS "EATS"	4.5×10^{4}	20	2.65	–	0.18	7×10^{-5}	–	–	1	2.5×10^{-2}	0.7×10^{54}
RS "model 1"	200	90	2.35	1.139	0.2	2×10^{-4}	380	–	0.52	–	1.6×10^{54}
RS "model 2"	200	90	2.35	0.518	0.2	6×10^{-5}	565	–	0.53	–	1.6×10^{54}
RS "EATS"	200	100	2.35	–	0.56	4×10^{-3}	–	–	1	2.5×10^{-2}	0.7×10^{54}

Note: Γ_{bulk} for the EATS model is that of photons emitted along the line-of-sight.